Mechanism for acetate formation in electrochemical $CO_{(2)}$ reduction on Cu: Selectivity with potential, pH, and nanostructuring

Hendrik H. Heenen,*,†,‡,¶ Haeun Shin,†,§ Georg Kastlunger,‡ Sean Overa,§ Joseph A. Gauthier, $^{\parallel,\perp,\#}$ Feng Jiao,*,§ and Karen Chan‡

† These authors contributed equally

‡ Department of Physics, Technical University of Denmark, DK-2800, Kgs. Lyngby,

Denmark

¶Fritz-Haber-Institut der Max-Planck-Gesellschaft, D-14195 Berlin, Germany

§Center for Catalytic Science and Technology, Department of Chemical and Biomolecular

Engineering, University of Delaware, Newark, DE, USA

∥SUNCAT Center for Interface Science and Catalysis, Department of Chemical

Engineering, Stanford University, Stanford, California 94305, United States

⊥SUNCAT Center for Interface Science and Catalysis, SLAC National Accelerator

Laboratory, 2575 Sand Hill Road, Menlo Park, California 94025, United States

#Present address: Department of Chemical Engineering, Texas Tech University, Lubbock,

TX 79409

E-mail: heenen@fhi.mpg.de; jiao@udel.edu

Abstract

Nanostructured Cu catalysts have increased the selectivities and geometric activities for high value C-C coupled (C₂) products (ethylene, acetate, and ethanol) in the electrochemical $CO_{(2)}$ reduction reaction $(CO_{(2)}RR)$. The selectivity among the highvalue C₂ products is also altered, where for instance the yield of acetate increases with alkalinity and is dependent on the catalyst morphology. The reaction mechanisms behind the selectivity towards acetate vs. other C₂ products remain controversial. In this work, we elucidate the reaction mechanism towards acetate by using ab-initio simulations, a coupled kinetic-transport model, and loading experiments. We find that trends in acetate selectivity can be rationalized from variations in electrolyte pH and the local mass transport properties of the catalyst and not from changes of Cu's intrinsic activity. The selectivity mechanism originates in the transport of ketene, a stable (closed shell) intermediate, away from the catalyst surface into solution where it reacts to acetate. While such a mechanism has not yet been discussed in $CO_{(2)}RR$, variants of it may explain similar selectivity fluctuations observed for other stable intermediates like CO and acetaldehyde. Our proposed mechanism suggests that acetate selectivity increases with increasing pH, decreasing catalyst roughness and significantly varies with applied potential.

Broader context

The electrochemical reduction of CO₂ enables the storage of renewable energy in carbon neutral fuels while simultaneously reducing greenhouse gas emissions. Recent developments have led to industrially relevant performances exploiting nanostructured Cu catalysts and gas-diffusion electrodes, which produce high value C₂ products at high current densities. The selectivity between these C₂ products, which mainly consist of ethylene, ethanol and acetate, still poses a challenge to maximize cost efficiency. In this joint experimental-theoretical work, we elucidate the selectivity mechanism towards acetate vs. ethylene and ethanol using a multi-scale modelling approach with excellent agreement to experiment. We determine that transport properties at the catalyst surface are pivotal in steering selectivity between acetate

and other C_2 products. While our insights deduce design rules for an acetate rich or poor CO_2 reduction process important for a pure liquid product stream, they can be generalized to understand selectivity changes with catalyst roughness of other products and processes.

Introduction

The electrochemical reduction of carbon dioxide (CO₂RR) or carbon monoxide (CORR) has the potential to enable the storage of renewable energy via the production of carbon neutral commodity chemicals. Cu electrocatalysts have thereby been extensively explored for $CO_{(2)}RR$, since Cu is the only material able to produce high value C-C coupled (C_2) products (ethylene, acetate, and ethanol). Improvements in activity and selectivity of these catalysts are urgently needed to enable the commercialization and cost-effective operation of CO₍₂₎RR electrolyzers.^{2,3} To this end, two key developments have been introduced over the last decade. Firstly, gas diffusion electrodes (GDE) in combination with flow cell setups achieve significantly higher current densities towards CO₍₂₎RR products over traditional H-cell setups, which suffer from mass transport limitations. 4-6 Secondly, various means of nanostructuring Cu have been explored in order to increase the active surface area and to tune the selectivity towards high value products. 1,7-10 For instance, nanostructured catalysts in a GDE/flow-cell setup have led to significantly increased selectivities towards acetate under alkaline conditions. 11,12 Originally considered a minor product, under these specific conditions, acetate has Faradaic efficiencies comparable to ethylene and ethanol, the two major C_2 products produced by Cu under neutral and mildly alkaline conditions. 4,11,13 To date, there is no consensus on how nanostructuring or mass transport impacts the intrinsic activity and selectivity of Cu towards the possible C₂ products. ^{9,10}

In this paper, we suggest that nanostructuring of Cu changes the selectivity for acetate vs. other C_2 products through altering the mass transport of products away from the electrode, and not through changes in intrinsic activity via new active sites. ¹² We suggest that

acetate forms via a solution reaction of ketene with OH⁻, which is heavily affected by transport and electrolyte pH. Our insight results from a comprehensive examination of reported experimental activities of Cu catalysts normalized to active surface area, an *ab-initio* derived microkinetic model coupled to mass transport, and through activity measurements on different Cu catalysts at a range of pH and loadings.

Previous computational studies have attempted to rationalize the acetate activity and selectivity through reaction thermodynamics and barriers. 11,12,14 However, the dependence of acetate selectivity on pH and potential remained an open question, and performance differences in various Cu samples were assumed to arise from different active sites. We suggest that such mechanisms are inconsistent with electrochemically active surface area (ECSA)normalized activity of all reported Cu catalysts and the potential dependence of observed selectivity. In contrast, our computational model shows that the interplay of kinetics and mass transport determines the acetate selectivity vs. other C₂ products. The model agrees with the experimentally observed trends in the dependence of acetate selectivity on potential, electrolyte pH, and catalyst roughness. Previously, transport limitations have already been suggested to alter selectivity behavior between CO₍₂₎RR products and H₂ by affecting reactant concentrations and local pH at the catalyst surface. ^{6,15–20} This work showcases how mass transport also controls the competition between the desorption and the further reduction of stable intermediates with a corresponding impact on selectivity. Such a concept has been similarly proposed for stable intermediates in ORR and methanol oxidation.²¹ This principle is, therefore, generalizable to controlling the selectivity of other stable intermediates in CO₍₂₎RR like CO and acetaldehyde. Overall, our combined analysis of experiments and simulations suggests that acetate selectivity against other C₂ products is optimized by a high interfacial and bulk pH and a low, microscopic surface roughness of the Cu catalyst, which should be considered in the design of $CO_{(2)}RR$ electrolyzers.

Results & Discussion

ECSA normalized current densities suggest no change in intrinsic activity to C₂ products with nanostructuring

We compare ECSA-normalized current densities, j_{ECSA} , to evaluate $\text{CO}_{(2)}\text{RR}$ activities and selectivities, in Fig. 1. j_{ECSA} is the best available estimate for the intrinsic activity in absence of mass transport limitations, as turnover frequencies (TOF), which reflect the true intrinsic activity per active site, are generally not accessible in electrochemical measurements. 1,10,22 Within the variations in active site densities amongst the catalysts considered, j_{ECSA} is proportional to the turnover frequency. 23

Fig. 1 shows j_{ECSA} for various Cu catalysts in both GDE and H-cell setups towards the sum of all C₂ products in CO₍₂₎RR and specifically to ethylene, ethanol, and acetate. Even under a wide range of reaction conditions (CO and CO₂ as the reactant, different electrolytes with pH ranging from 6.8 to 14.3, wide potential range) and catalyst morphologies (from Cu single crystals and foils to deliberately roughened oxide-derived (OD) Cu, nanowires and nanoparticles) we find the currents to overlap within an order of magnitude for data sets without obvious transport limitations (blue lines in Fig. 1, which all correspond to GDE setups). H-cell setups, where transport limitations are present at lower overpotentials (gray lines in Fig. 1), show larger deviations.

Recent reviews have pointed out the similar intrinsic activities amongst different types of Cu catalysts towards all $CO_{(2)}RR$ products. ^{1,10} We confirm this observation in Fig. 1, and, in addition, we highlight the similar activity of different Cu catalysts towards the individual major C_2 products. The minor variation in partial current densities in Fig. 1 suggests a uniform intrinsic activity towards the different products and therefore the same active site on the different catalysts (when following typical preparation procedures ²⁴). If the order-of-magnitude change in partial current densities were to arise instead from a change in active site, the difference in the activation energies towards a given product would be around \leq

0.05-0.10 eV, assuming similar active site densities (and following the Arrhenius law). The expected electronic effects of changing an active site are, however, usually between 0.3 and 1.0 eV^{23} and would result in significantly larger variation (Δ) of 5 to 15 orders of magnitude in the TOF and corresponding partial current densities. Such large variations stand in contrast to the minor variations (Δ) of factor 4 to 21 as indicated in Fig. 1. Therefore, we hypothesize that possible changes in selectivity (contained in minor variations in activity between different C_2 products) arise only due to changes in active site densities (or respectively, the uncertainty in the determined ECSA), electrolyte pH or transport limitations.

Fig. 1 also shows a subtly stronger variation of the acetate currents in comparison to ethylene and ethanol although all C_2 products follow a similar potential behavior (or Tafel slope). While the former is a function of the electrolyte pH and catalyst morphology (see below), the latter indicates the same rate determining step for these C_2 products. In what follows, we derive a comprehensive mechanism for acetate which rationalizes the dependence of its activity on pH and catalyst morphology.

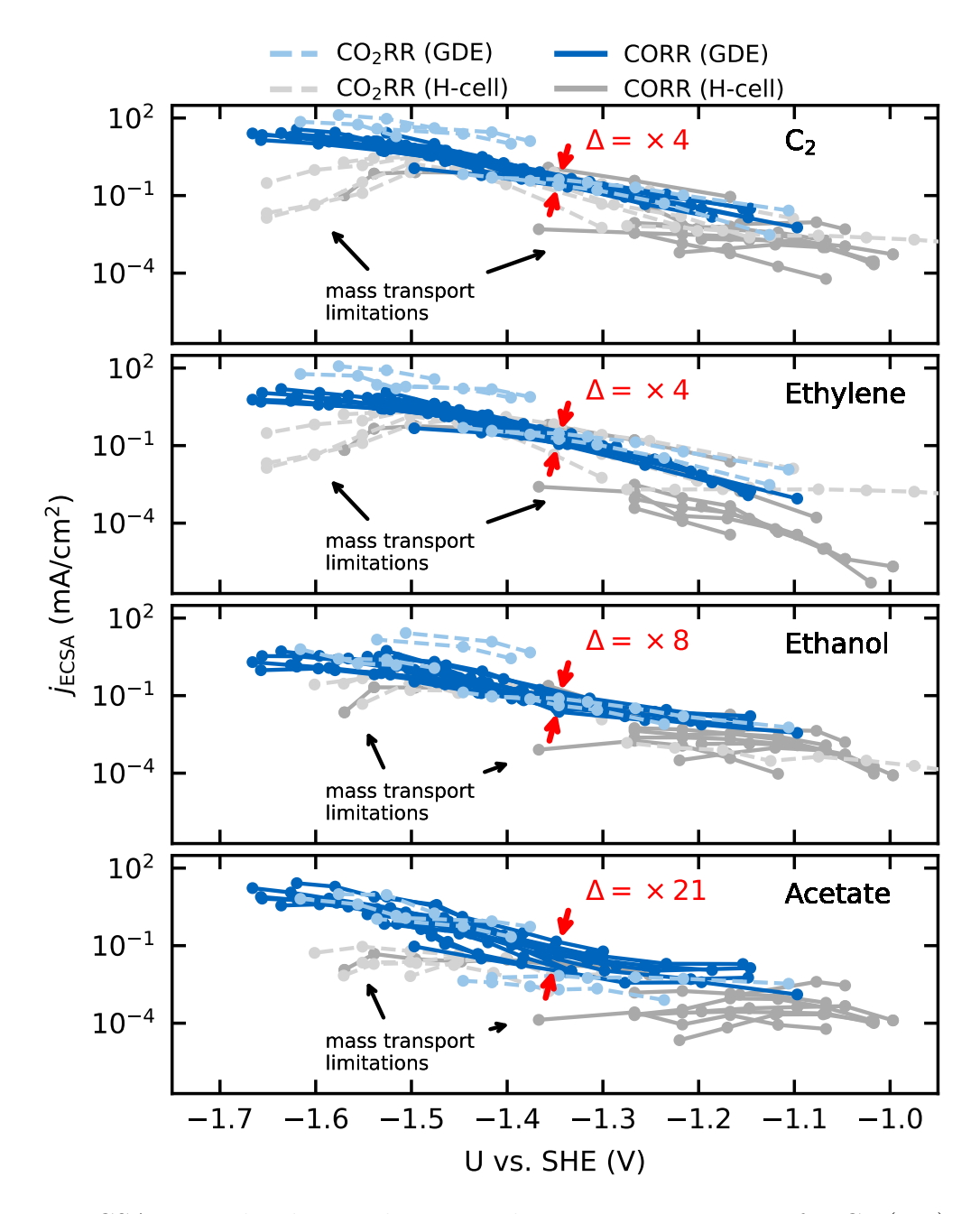


Figure 1: ECSA normalized partial current densities against U_{SHE} for C_2 (top), ethylene (upper center), ethanol (lower center), and acetate (bottom) adapted from different CO_2RR (dashed lines) and CORR (solid lines) studies conducted in a GDE/flow-cell setup (light-blue / blue) or a conventional H-cell setup (light-gray / gray). Each line represents an individual data set of same reaction conditions. The GDE data is adapted from 4, 11, 25–29 and the H-cell data from 7, 8, 30, 32, 33. The red arrows indicate the (multiplicative) factor in variation of j_{ECSA} (Δ) at -1.35 U_{SHE} .

$Ab\ initio$ calculations suggest a solution phase reaction of ketene and OH^- towards acetate

Fig. 2 shows our proposed mechanism of the selectivity determining steps (SDS) towards acetate vs. other major C₂ products, determined on the basis of DFT simulations. Central to this mechanism is the ketene intermediate as suggested previously. ^{8,11,14} However, we emphasize its importance in both its desorbed (H₂CCO(aq)) and adsorbed (H₂CCO*) state. As shown in Fig. 2, a proton-coupled electron transfer (PCET) to HCCO* leads to the formation of the stable ketene molecule, desorbed from the surface. This reaction step is pivotal because past its formation, H₂CCO(aq) can either react with OH⁻ to acetate in solution (a well-known reaction ³⁴) or readsorb and get further reduced to other C₂ products. Either pathway is differently influenced by pH, (ketene) transport, and potential. The elementary reactions making up this branching point evolve around two SDS as indicated in Fig. 2:

- 1. (SDS-surf, only low overpotentials) The PCET reaction of H_2CCO^* towards other C_2 products vs. the desorption of re-adsorbed ketene
- 2. (SDS-sol) The solution reaction vs. re-adsorption of desorbed ketene

Firstly, we note that SDS-sol is dependent on the concentration of H₂CCO(aq) and OH⁻ at the catalyst surface which depends strongly on mass transport. Secondly, we note that SDS-sol involves the competition between two chemical steps while SDS-surf between a chemical and an electrochemical step. Acetate selectivity of SDS-sol is therefore not (directly) potential dependent in contrast to SDS-surf. The concentration and potential (in)dependence have an important impact on the selectivity, as we detail below.

We derived and validated this mechanism using density functional theory (DFT) calculations. In our derivation, we assume the same rate determining step (RDS) for all C₂ products based on previous experimental and theoretical studies, which has been suggested to either be a CO* dimerization^{35–37} or the protonation of the OCCO* intermediate with water as the proton donor.³⁸ The same RDS is consistent with the range of similar Tafel

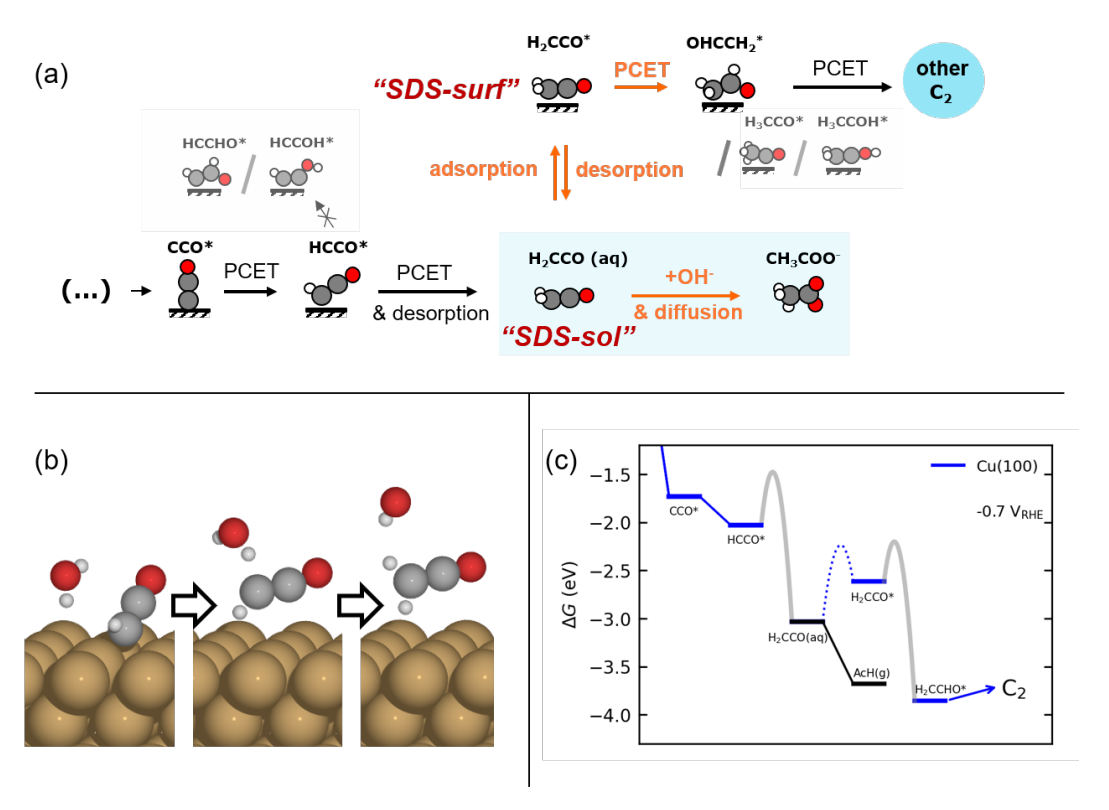


Figure 2: (a) Schematic of the Ketene pathway. We show the mechanism we investigated in our model, i.e. after the RDS and including the two selectivity-determining steps, "SDS-sol" and "SDS-surf" towards acetate via a solution reaction or the further reduction of the adsorbed ketene (H_2CCO^*) to form other C_2 products. We also depict the excluded alternative reduction steps. (b) Illustration of the simultaneous desorption and reduction of $HCCO^* \rightarrow H_2CCO$ (aq) on Cu(100) as obtained from NEB simulations. (c) Free energy diagram for the suggested ketene pathway on Cu(100) at -0.7 V vs. RHE (pH=14). Depicted is the considered division into the pathways including reduction of H_2CCO^* (blue) and the desorption of ketene and its hydrolysis to acetate (black), respectively. The adsorption barrier of ketene (dotted) and the approximated electrochemical barriers (gray, see methods) are shown. Free energy diagrams for Cu(111), Cu(110), and Cu(211) are shown in Fig. S12.

slopes and the distinguishing lack of an inverse pH-activity relationship shared among the considered C₂ products (acetate, ethanol, ethylene)¹¹ (see Fig. 1 above and elaboration of the pH effect in the SI Sec. 6). Such a shared and early RDS means that energetics of following intermediates have no effect on the activity towards the sum of all C₂ products, and only affect the selectivity amongst them (i.e. $r_x = r^{\text{RDS}} \frac{r_x^{\text{SDS}}}{\sum_i r_i^{\text{SDS}}}$, with x being a specific product of the SDS).³⁹ We evaluate our suggested reaction mechanism on representative facets: Cu(111) and Cu(100) terraces and Cu(110) and Cu(211) as steps. We choose intermediates prior to HCCO* (and thus ketene) based on their thermodynamic or kinetic stability which is in line with established trends. 40 On all facets considered, the free energies of all steps are mostly downhill and any uphill step is well below 0.75 eV as shown in Fig. 2c and S12 which makes the mechanism feasible at room temperature.²³ We also evaluated the chemical and PCET barriers at a constant potential 41 (see methods and Sec. 3 in the SI) around SDS-sol and SDS-surf which are also low enough to lead to measurable rates at room temperature (see Fig. 2c, and Fig. S12 and Tab. S6 in the SI). An only exception is an insurmountable re-adsorption barrier for ketene on Cu(111) and Cu(110), which makes these facets inactive for the proposed mechanism to other C₂ products (see Fig. S12 and Sec. 5.6 in the SI). We emphasize that the direct $HCCO^* \rightarrow H_2CCO(aq)$ step was an explicit result from the transition state search and occurs on all investigated facets.

Acetate selectivity is determined by the interplay of kinetics, mass transport, and electrode roughness

To investigate the selectivity behavior we couple our DFT-based energetics with both a microkinetic and a mass transport model. The microkinetic model describes the surface reactions of our proposed reaction mechanism to acetate and other C₂ products (see Fig. 2 and SI Sec. 5.1). The mass transport model describes the transport according to the conditions of CORR operation in a GDE/flow cell setup (with corresponding pH, reactants, and diffusion lengths), where the highest selectivity for acetate is observed. ^{4,8,11,25,30} We only

consider the dominant pathway for the acetate formation (i.e. $CO_{(2)}RR$ at cathode) in this study, although acetate could also be formed through a partial oxidation of ethanol (the product of $CO_{(2)}RR$) at the anode in certain cell configurations due to its cross-over through membranes.^{25,42}

In our microkinetic model we fit the common RDS for the C₂ products to the ECSA normalized activity found in experiment (see SI Sec. 5.1). Further, we apply our DFT-derived energies for Cu(100) in the microkinetic model, whereby the quantitative behavior of the model is only sensitive to the re-adsorption, desorption, and reduction barrier of the ketene intermediate and insensitive to any other facet dependent energy (see SI Sec. 5.6). We note that we fitted the free energy of H₂CCO(aq) at the interface to reproduce the experimental selectivity, as it is poorly represented by the static electrode-solvent interface applied in our calculations. This fit leads to an energy correction of 0.29 eV which is within DFT uncertainty on the one hand but also reproduces the adsorption barrier height on Cu(211) on the other hand, and is therefore a reasonable assumption (see SI Sec. 5.6.1, Fig. S18).

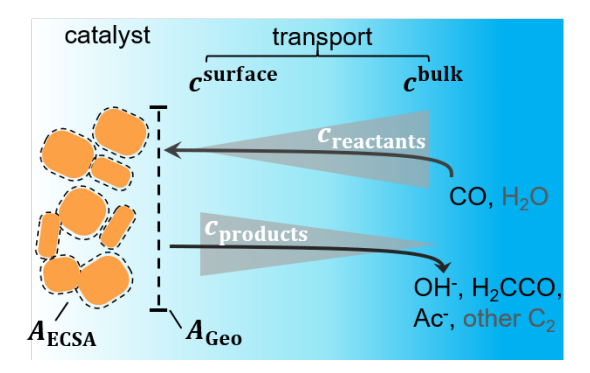


Figure 3: Schematic of the mass transport considered in our model. CO, OH⁻, H₂CCO, and Ac⁻ (black color) are considered for transport while H₂O and other C₂ are neglected (grey color). Typical concentration gradients are depicted and it is indicated how the transport scales with geometric area A_{Geo} while processes on the catalyst surface scale with A_{ECSA} .

For the description of the mass transport, we use a 1D-mass transport model where we account for the diffusion of CO, OH⁻, and H₂CCO as well as the solution reaction of H₂CCO and OH⁻ to acetate, ^{19,43} as illustrated by Fig. 3 and S14. We also include a Sherwood

relation to account for the convective mass transport encountered in a flow cell. It describes the diffusion of species from the bulk of the flowing electrolyte to the electrode surface. $^{44-46}$ All constants and coefficients are taken from literature, for details we refer to the methods section and SI Sec. 5. Within our 1D approximation, the effect of the nanostructuring of Cu is captured only by a single roughness factor ρ , and we assume a constant active site density. The roughness ρ generally describes the ratio of active area and geometric area $(A_{\rm ECSA}/A_{\rm geo})$. This ratio can change microscopically with local curvature and porosity of the nanostructured Cu surface or mesoscopically with the loading of Cu particles on the GDE. As discussed in detail later, the short diffusion length scales in the presence of the rapid solution reaction treated here, effectively define ρ to be a microscopic roughness.

The included mass transport limitations give rise to changes in the microscopic reaction environment at the catalyst surface through changes in the surface concentrations of individual species (in our case of CO, OH⁻, and H₂CCO). Their local concentrations decisively affect the coupled reaction kinetics. For example, increasing flux and current densities at higher overpotentials give rise to increased concentration gradients, such that the surface concentrations of reactants (CO) decrease while those of the electrochemical products (OH⁻ and H₂CCO) increase (compare Fig. 3). The concentration profiles are further affected by pH and ρ as discussed in detail in the SI Sec. 5.5 which importantly influence acetate selectivity trends. These relations finally enable the simulation of the C₂ current and selectivity in dependence of potential, bulk pH and catalyst roughness ρ as depicted in Fig. 4a.

The simulated geometric current densities of C_2 products $(j_{\text{geo}}^{C_2})$ are shown in the top panel of Fig. 4a. The maximum $j_{\text{geo}}^{C_2}$ reached at high overpotentials (more negative U) reflects the CO diffusion limited current density (see Fig. S17a showing the depletion of CO close to the surface). At lower overpotentials, the linear dependence of $j_{\text{geo}}^{C_2}$ on the catalyst ρ reflects the linear dependence of $j_{\text{geo}}^{C_2}$ on A_{ECSA} .

The bottom panel in Fig 4a shows the computed selectivity of acetate vs. the total C_2 products $(S_{Ac^-}^{C_2})$. We emphasize that the shown selectivities, being molar ratios relating

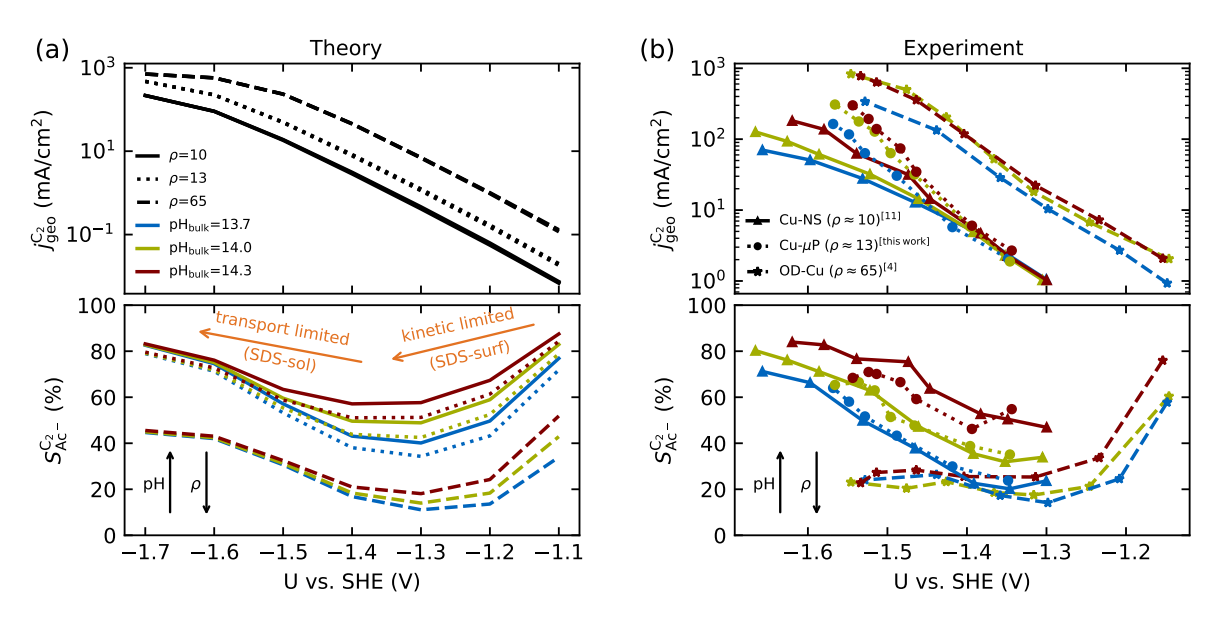


Figure 4: Geometric current densities towards all C_2 products $(j_{geo}^{C_2}, \text{ top})$ and acetate selectivity among them $(S_{Ac^-}^{C_2}, \text{ bottom})$ against U_{SHE} as simulated by our transport coupled microkinetic model (a) and experimentally measured (b). Each line represents an individual data set with the same reaction conditions. The different colors represent varying electrolyte pH and the solid, dotted, and dashed lines experiments and simulations with Cu-NS or $\rho = 10$, Cu- μ P or $\rho = 13$, and OD-Cu or $\rho = 65$, respectively. The experimental data has been measured in this work or is adapted from 4, 11. Note that the simulated $j_{geo}^{C_2}$ is invariant to pH as it follows the pH independent RDS of the C_2 products and competition to C_1 and HER or cation effects 47 are not included in our model, the simulated $j_{geo}^{C_2}$ is therefore depicted in black. The simulated $j_{geo}^{C_2}$ for $\rho = 10$ was scaled by $\frac{1}{2}$ according to the lower loading used for the CU-NS of 0.5 mg cm⁻² compared to 1.0 mg cm⁻². 4,11 The dominating selectivity mechanisms including kinetic and transport competition are indicated (see text).

between C_2 products, differ from Faradaic efficiencies (FE) which are weighted by transferred electrons and therefore ambiguous for a mechanistic analysis. In general, we distinguish the critical variables affecting $S_{Ac^-}^{C_2}$ as the roughness ρ and the (interfacial) pH. These variables depend on catalyst morphology and on electrolysis conditions. Resulting trends arise from the competition between the transport/solution reaction and re-adsorption of $H_2CCO(aq)$ in SDS-sol (see Fig. 2a):

- An increasing roughness ρ lowers $S_{\text{Ac}^-}^{\text{C}_2}$ since an increased catalyst surface area (A_{ECSA}) favors $\text{H}_2\text{CCO}(\text{aq})$ adsorption. Note that the area which affects transport and solution reaction towards acetate (A_{geo}) remains unchanged.
- An increasing concentration $[OH^-]$ increases $S_{Ac^-}^{C_2}$ since OH^- catalyzes the solution reaction of ketene to acetate. This selectivity behavior confirms a first order dependence of acetate formation with OH^- . The interfacial pH (which scales with the bulk pH) is decisive because the conversion of ketene occurs close to the catalyst surface (as elaborated below).

 $S_{\mathrm{Ac}^{-}}^{\mathrm{C}_{2}}$ scales stronger with the roughness and weaker with pH (compare Fig. 4) following the relation

$$S_{\rm Ac^-}^{\rm C_2} \propto \frac{\sqrt{\rm [OH^-]}}{\rho}$$
 (1)

as we derive in the SI Sec. 7. The U-shaped selectivity curve vs. potential can be explained by the interplay of SDS-sol and SDS-surf.

- (i) At low overpotentials: The selectivity towards other C₂ products is limited by the potential dependent protonation of H₂CCO* (in SDS-surf) while the step towards acetate is potential independent. Therefore, as the overpotential increases, the selectivity towards acetate decreases.
- (ii) At high overpotentials: The protonation of H₂CCO* is facile. The selectivity is then determined by H₂CCO(aq) readsorption vs. the solution phase reaction of H₂CCO(aq)

with OH⁻ (in SDS-sol). The build-up of local OH⁻ concentration at increasing overpotentials (local pH, see concentration profile in Fig. S17b) favors the latter reaction and leads to an uptick in acetate selectivity.

The complex selectivity behavior of our simulations is consistent with experiments as shown in Fig. 4b. We compare to experimental data measured in this work and data adapted from 4, 11 which is based on conditions equivalent to our simulations (CORR in a GDE/flowcell setup). Different Cu-catalyst morphologies are included in this data with nanosheets (Cu-NS), micron sized particles ($Cu-\mu P$), and oxide-derived Cu (OD-Cu). The roughness of these catalysts was determined to be 10, 13, and 65, respectively, via capacitance measurements and after normalization by loading (see SI Tab. S5). 4,11 At comparable catalyst loadings for these samples, the differences in the roughness should arise for the most part from microscopic variations amongst the catalysts' morphology. We therefore apply these roughness values to be the microscopic roughness ρ in our model. We find $j_{\rm geo}^{\rm C_2}$ to align between theory and experiment regarding the limiting behavior of CO diffusion and the scaling with respect to ρ , which is expected as a direct result of the fitted RDS. Importantly, as a consequence of the proposed mechanism, the simulated acetate selectivity $S_{\mathrm{Ac^{-}}}^{\mathrm{C}_{2}}$ shows a very good agreement with experiment. We observe the same trends in roughness and electrolyte pH for the acetate selectivity $S_{
m Ac^-}^{
m C_2}$, i.e. increasing $S_{
m Ac^-}^{
m C_2}$ with decreasing roughness and increasing pH. Also, the complex potential dependent U-shape is found in both simulated and measured data. We note that this U-shape is not only observed in the acetate selectivity among C_2 products $(S_{Ac^-}^{C_{2+}})$ shown here but can also be seen in acetate's Faradaic efficiency (see SI Fig. S1).

We note that at higher overpotentials, there is a pH dependence of activities (partial current densities $j_{\text{geo}}^{C_2}$) in the experimental data in the upper panel of Fig. 4b. We note that we did not include the competing pH dependent C_1 pathway or ion concentration effects ^{1,47} in our simulations which could reproduce such an apparent pH dependence. Other/smaller quantitative deviation may originate in uncertainty of the measured catalyst roughness, of assumed flow-rates and of the charge-neutral approximation or neglected size effects in our

Short diffusion lengths of ketene suggest that micro-, not macroscopic roughness determines acetate selectivity

As we show in Fig. 5a, the diffusion length L_d for $\mathrm{H_2CCO}(\mathrm{aq})$ is within 200 nm of the catalyst surface due to the rapid solution reaction between $\mathrm{H_2CCO}$ and $\mathrm{OH^-}$. This length scale is not only well within a diameter of a single pore of a GDE electrode 6,17,45 but on the same order of magnitude as the diameter of the catalyst particles (d_P) used for the experiments in Fig. 4b (see SI Fig. S2 and 4, 11). Thus, in such an electrode arrangement the diffusion spheres around the nanoparticles do not overlap as we show in Fig. 5c. Instead, the length scale of roughness features relevant for the competition between kinetics and mass transport in our selectivity mechanism are smaller than d_P . We therefore define ρ in our model as a microscopic roughness $A_{\mathrm{real}}/A_{\mathrm{smooth}}$, where A_{smooth} corresponds to the area of an ideal, smooth nanoparticle. This definition of the roughness fulfills its general definition $A_{\mathrm{ECSA}}/A_{\mathrm{geo}}$, but not vice versa. Thus, changes in catalyst loading (which alter $A_{\mathrm{ECSA}}/A_{\mathrm{geo}}$) do not alter ρ and should therefore lead to no changes in the acetate selectivity. This is true unless the diffusion spheres of adjacent particles could overlap significantly which would be the case for very small nanoparticles ($d_P << 100$ nm) (compare Fig. 5c).

We evaluated this hypothesis through our measurements of CO reduction in 1M KOH on Cu catalysts of different morphology and at different loadings. Specifically, we compare micron-sized (Cu- μ P, same as above) and 25nm-sized (Cu-25nmP) particles which we characterize with a mass normalized roughness ρ of 13 and 63, respectively (see SI Sec. 1.5). Note that by changing only the loading of Cu particles, the morphology of the catalyst and its microscopic surface roughness ρ remain the same. With higher loadings, the geomet-

ric current densities increase (which necessitates measurements at different potential ranges for matching current densities), but the current densities coincide after mass normalization (see Fig. S5). This alignment with normalization suggests that the higher current densities at higher loadings are due to the increased active area with the same intrinsic activity. As shown in Fig. 5b, the same selectivity of acetate among the C_2 products $S_{Ac^-}^{C_2}$ is found within the range of 0.5-1.5 mg cm $^{-2}$ and 1.0-1.5 mg cm $^{-2}$ for Cu- $\mu\mathrm{P}$ and Cu-25nmP, respectively. While $S_{\rm Ac^-}^{\rm C_2}$ is independent of these loadings, it still differs according to the mass normalized roughness ρ and hence according to the catalyst morphology, in line with our computational model (compare Fig. 4a and Fig. S4). These trends in $S_{\rm Ac^-}^{\rm C_2}$ confirm that it is not the loadingdependent mesoscopic roughness but the morphology dependent microscopic roughness (ρ) that affects the selectivity towards the solution reaction. In correspondence to our predicted length scales in Fig. 5a, we do, however, see a loading dependence at very low loadings for the very small Cu-25nmP. Decreasing the loading progressively to $0.5~{\rm and}~0.3~{\rm mg~cm^{-2}}$ we find an increasing $S_{Ac^-}^{C_2}$. We hypothesize that, at such low loadings the overlap of diffusion lengths (L_d) between particles decreases with loading since each particle has statistically fewer neighbors. This in turn noticeably lowers the effective surface area at the length scales relevant to the solution reaction, i.e. ketene has less (local) surface to re-adsorb, subsequently increasing $S_{\rm Ac^-}^{\rm C_2}$. At higher loadings the amount of neighbor particles saturates similar to a packing limit (leading to uniform selectivity with increasing loading). This particle size effect is very sensitive because we do not find any noticeable loading dependency for the slightly larger 40-60 nm sized Cu particles (Cu-50nmP) which are additionally shown in the SI (Sec. 1.4-1.5). From these particle sizes onward, the local surface area gained by particle overlap is negligible compared to the particles area at the solution reaction length scales (see Fig. 5c).

While our findings highlight the importance of the local, microscopic variations in the structure of the Cu catalysts we emphasize that this relevance arises from the rapid solution reaction which leads to a very short diffusion length (compare Fig. 5). For intermediates

that do not react in solution it has been shown in ORR (for H₂O₂) and methanol oxidation (for formaldehyde and formic acid) that the mesoscopic roughness (hence the loading) also influences their degree of re-adsorption and further reduction or oxidation, respectively.²¹ This difference is due to the larger diffusion lengths expected for pure diffusion processes.

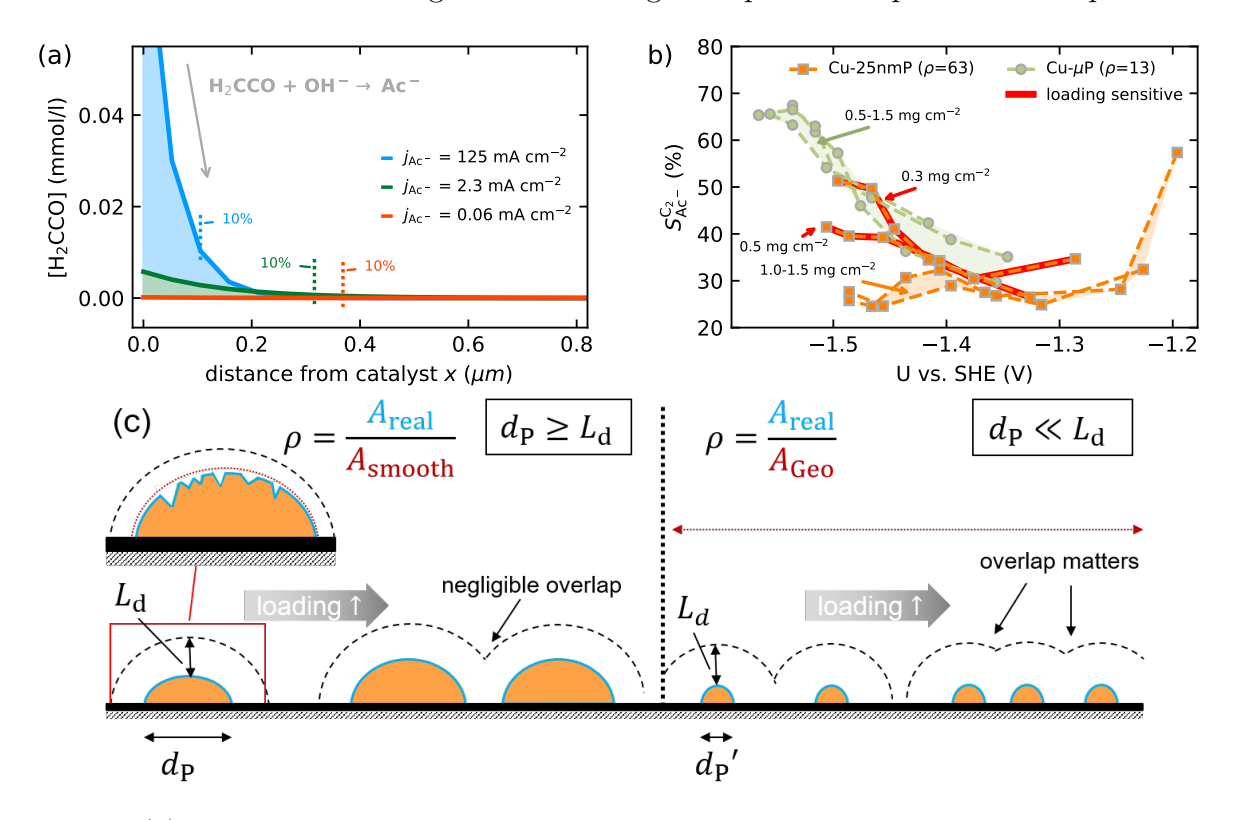


Figure 5: (a) Concentration profile of ketene against distance from the catalyst indicating the length scales of its conversion to acetate as given by our mass transport model at different partial current densities for acetate. The vertical lines indicate the distance where 90% of ketene has reacted to acetate. (b) Acetate selectivity among all C_2 products ($S_{Ac^-}^{C_2}$) against U_{SHE} for experiments in a GDE with different loadings of Cu- μ P and Cu-25nmP. Each line represents an individual data set of same reaction conditions. The shaded regions show the loading-independent selectivity ranges. The red highlighted lines are the loading dependent data found for the small Cu-25nmP. (c) Illustration of the effect of the diffusion length L_d in comparison to the particle diameter d_P , loading and the roughness ρ relevant to transport effects. At short L_d the overlap of diffusion spheres is negligible and only the local roughness matters (compared to a smooth particle surface). At long L_d diffusion spheres overlap and loading affects selectivity.

Why alternative pathways are unlikely

Since our mechanism in Fig. 2 is derived from DFT simulations, there may be inherent errors in the predicted energetics⁴⁸ and barriers and therefore uncertainties in the resultant pathways. Supporting our suggested mechanism, we discuss here why previously proposed ^{11,12,14} and other alternative pathways are unlikely from a theoretical analysis of the experimentally observed pH and potential dependence in the activity.

Acetate selectivity cannot be determined by a PCET. The pH dependence of acetate in comparison to other C₂ products is only possible with OH⁻ as a reactant in contrast to a recent study ¹² which proposed an early PCET reaction as the SDS towards acetate. On a potential vs. SHE scale, PCET reactions in alkaline conditions, where water is a proton donor, are either pH independent ⁴⁹ (where the RDS is the first PCET) or show a decrease in activity as pH increases (where the RDS is the 2nd or later PCET) ³⁸ (also see SI Sec. 6). In contrast, as shown in Fig. 4, the activity for acetate increases with pH in relation to other C₂ products. Since the C₂ products do not depend on pH on an SHE scale ^{1,38,50} (or have even an apparent increasing activity with pH as visible in the upper panel of Fig. 4b) it follows that the SDS of acetate must in turn have an intrinsic pH dependence (which is greater than the apparent C₂ one). This is only possible if OH⁻ is a reactant in the SDS, since the involvement of OH⁻ would lead to the necessary intrinsic pH dependence when involved in any reaction step prior to, coinciding with, or after the RDS.

Acetate does not have a RDS separate from other major C_2 products. Our assumption of a shared RDS between acetate and other C_2 products is the most likely scenario and has also been assumed in previous work. ^{11,12,14} As Fig. 1 shows, the total C_2 's, ethanol, ethylene, and acetate follow the same experimental trends: They share similar Tafel slopes (see 11 and Fig. 1) and do not follow an otherwise distinguishing inverse pH-activity relationship (see SI Sec. 6). ³⁸ Further, an alternative separate RDS of acetate would need to be a potential dependent reaction involving OH^- on the catalyst surface to yield the pH and potential dependence in acetate activity. Such a reaction step would, however, correspond to an oxidation reaction

since OH⁻ would need to discharge.

The SDS for acetate does not involve OH^- in a surface reaction. Alternative to our suggested solution reaction, a hydrolysis on the catalyst surface has been suggested. ^{11,14} This reaction would imply a nucleophilic attack of OH^- occurring on the negatively charged surface onto H_2CCO^* (or another early intermediate). Such a step appears highly improbable due to electrostatic repulsion, oxidative nature of the process and limited steric accessibility of the surface bound carbon atoms in those intermediates. Simulating this reaction for H_2CCO^* , we indeed find it associated with a high reaction barrier of $\Delta G^{\dagger} = 0.8 \,\mathrm{eV}$ and potential dependence which is inconsistent with the experimental behavior (see SI Sec. 3.2).

The selectivity determining step(s) for acetate do not involve competing PCET vs. chemical reaction steps at high overpotentials. Refs 12 and 14 have, on the basis of reaction thermodynamics and barriers, suggested the selectivity towards acetate to be solely determined by the competition between a chemical surface reaction towards acetate vs. a PCET towards other C_2 products. However, this mechanism is unlikely because the PCET step towards other C_2 products would increase exponentially with increasing potential, which would result in negligible amounts of acetate, whose TOF would be potential independent (compare potential dependence SDS-surf). In contrast, our proposed SDS-sol includes competition between H₂CCO re-adsorption and a solution reaction, where neither of these steps are PCET. This non-PCET dependence in SDS-sol compensates the potential dependence of the consecutive SDS-surf. The corresponding coupled transport-kinetic model (Fig. 4) shows significant selectivities for both acetate and C₂'s over a wide potential range consistent with experiments. A Cannizzaro-type reaction is less likely than ketene hydrolysis in solution phase. The Cannizzaro reaction has been suggested as a possible source for acetate formation. 51-53 Since this solution-based disproportionation reaction of acetaldehyde to acetate and ethanol is also OH⁻ catalyzed, it would yield the same trends with pH and roughness as ketene hydrolysis. It would, however, also yield a 50:50 ratio of ethanol and acetate which is never found experimentally. Even if a substantial part of the additional ethanol would be oxidized to acetate at the anode, ^{25,42} a slightly increased ethanol yield with pH and roughness should still be expected. Experimentally, the opposite trend is found, ^{11,12} which renders this mechanism unlikely.

Ketene hydrolysis in solution best explains experimental observations. The proposed solution reaction of ketene is in line with $C^{18}O^4$ and $H_2^{18}O^{52}$ isotope labeling experiments and a recent study where amines are co-feed to CORR. ¹⁴ For the latter, a competing solution reaction of ketene with OH^- or amines explains the studies' selectivity trends with potential, pH, and amine identity.

The proposed mechanism is not specific to reaction conditions. Our proposed mechanism and its implications are valid for both CORR and CO₂RR. However, the latter usually contains a reduced local pH due to the equilibrium of CO₂ with bicarbonate⁴ which gives rise to low acetate yields. A notable exception are highly alkaline electrolytes, e.g. 10M KOH (pH \approx 15) where high acetate yields are observed for CO₂RR.¹³ Similarly, high yields of acetate at high overpotentials are less often seen in H-cell experiments, since high current densities are not achievable which would lead to the necessarily high local pH values (pH \geq 14-15, compare SI Fig. S16).

The ketene pathway is most likely the main C_2 pathway. We assume in our computational model that all C_2 products go through the ketene mechanism. This assumption is supported by acetate selectivities > 80 % and direct FE competition between acetate and all other C_2 products in the experiments of Refs 4, 11 as shown in Fig. 4. Contrary to these observations, recent experiments at very negative potentials of < -1.9 V_{SHE} showed that acetate can be obtained as the sole liquid product, out-competing nearly all ethanol, while ethylene is less affected. Our DFT simulations can also not provide a clear picture in that matter. An early bifurcation from the ketene pathway via the reduction of HCCO* to HCCOH* instead of H_2 CCO (aq) at very high overpotentials may be likely, but within the typical DFT error very uncertain (see SI Sec. 3.1). While most available data at low overpotentials or/and highly alkaline conditions 4,8,11,14,31,42 suggests that the ketene pathway is the main C_2 pathway,

we cannot exclude other pathways. However, the uncertainty about additional mechanisms does not affect the preceding arguments about selectivity since the contribution of any prior bifurcation must be small, given the overall high acetate yields.

Conclusion

In summary, we have presented a novel mechanism towards acetate in $CO_{(2)}RR$ based on the solution reaction of ketene which elucidates the dependence of its selectivity on potential, pH and microscopic roughness. We gained this insight by an analysis of available GDE/flow cell and H-cell data, an experimental investigation of the effect of catalyst loading, and with the development of a multiscale model that predicts trends in selectivity vs. roughness, pH, and potential consistent with experiment. Our proposed mechanism dictates that the acetate selectivity is determined by the transport and subsequent solution reaction of ketene vs. its (re-)adsorption and further reduction at the catalyst surface.

We emphasize that we have not invoked any special active site(s) towards acetate specific to a catalysts' morphology in our model; the effect of nanostructuring is captured by a single roughness parameter relevant at nm length scales consistent with experiment. The effect of roughness arises from its influence on the interplay between transport and kinetics. Our examination of available ECSA-normalized data on nanostructured Cu suggests that active site(s) to be same across all types of Cu investigated thus far.

Based on our insight from the elaborated mechanism, we propose the following strategies to maximize or minimize acetate yields: Generally, a high pH, a low catalyst roughness, and very high (\geq -1.2 V_{SHE}) or very low potentials (\leq -1.5 V_{SHE}) maximize the acetate yield. For highest acetate yield, the reaction should occur at low potentials and/or in very alkaline CORR conditions, similar as exploited in recent work. ^{11,12,42} In contrast, a low acetate selectivity follows an operation of a very rough catalyst in neutral conditions using a buffer and intermediate potentials (-1.6 to -1.3 V_{SHE}).

The presented mechanism rationalizes the trends in acetate selectivity based on the transport of stable intermediates/products. We note that a similar transport related process may also be relevant for other stable intermediates in $CO_{(2)}RR$ like CO and acetaldehyde as also suggested by operando mass spectrometry experiments. ^{53,54} This work highlights the importance of a rigorous evaluation of intrinsic catalyst activities and the potential impact of the interplay of reaction energetics, solution phase reactions, and mass transport in mechanistic studies of $CO_{(2)}RR$ and beyond. From a simulation perspective, the combination of these effects on multiple length scales requires rigorous multiscale models beyond usual approaches focusing only on the reaction energetics on the catalyst surface.

Methods

Electrode preparation

The experiments were conducted using commercial micron-sized Cu particles (Cu-muP, Alfa Aesar) and 40-60 nm Cu particles (Cu-50nmP, Sigma-Aldrich) and 25 nm Cu particles (Cu-25nmP, Sigma-Aldrich) as a cathode with NiFeO_x as an anode. To prepare the cathode catalyst ink, 35 mg of copper powder was dispersed in 3 ml of isopropanol and 50 μ l of Nafion ionomer (5 wt% in H2O, Fuel Cell Store). The ink was drop-casted onto Sigracet 39 BB GDL (Fuel Cell Store) to a loading of 1.0 mg cm⁻² for the electrolyte pH test. For the loading test, the loading was varied from 0.3 to 1.5 mg cm⁻². The anode was prepared via an electrodeposition method on the cleaned nickel foam following a previous report. The nickel and iron ions were deposited onto the cleaned nickel foam at a potential of -1.0 V vs. Ag/AgCl for 5 minutes in a mixture solution of 3 mM Ni(NO₃)₂:6H₂O (Sigma-Aldrich) and Fe(NO₃)₃:9H2O (Sigma-Aldrich). A platinum wire was used as a counter electrode in this preparation.

CO electrolysis

All CO electrolysis was performed in a three-channel flow cell. The dimension of the channel was $2 \text{ cm} \times 0.5 \text{ cm} \times 0.15 \text{ cm}$ with 1 cm^2 geometric area of the electrode exposed to the electrolyte flow. The cathode and anode were separated by an anion exchange membrane (FAA-3-50, Fumatech) activated in 1 M KOH (99.98% metal basis, Alfa Aesar) overnight. The CO was fed into the electrolyzer at a 10 sccm flow rate controlled using a mass flow controller. Aqueous KOH solution was fed into each analyte and catholyte chamber. The catholyte flow rate was set to 0.6 ml min⁻¹ without circulation while the analyte flow rate was set to 1 ml min⁻¹ to facilitate oxygen flow generated from the oxygen evolution reaction at the anode. Each electrode had direct contact with the electrolyte as the electrolyte flowed. The cathode potential was measured using an external Hg/HgO reference electrode (4.24 M KOH, Koslow Scientific) and converted to the standard hydrogen electrode (SHE) scale with 100% iR correction $E(vs.SHE) = E(vs.Hg/HgO) + 0.098V - \eta_{iR}$. During the electrolysis, the gas products (i.e. hydrogen, ethylene and methane) were transferred through HaySep D and Molsieve 5 Å columns and identified/quantified with a thermal conductivity detector and a flame ionization detector on a Multiple Gas Analyzer no. 5 gas chromatography (SRI Instruments). The liquid products (i.e. acetate, ethanol and n-propanol) were collected from the outlet of the catholyte for 5 minutes at each potential and quantified by ¹H NMR spectroscopy (Bruker AVIII 600 MHz NMR spectrometer) using 25 ppm dimethyl sulfoxide (Alfa Aesar) in D₂O (Sigma-Aldrich) as an internal standard.

Material characterization

The surface structure of the cathode catalysts was characterized using a Zeiss Auriga-60 scanning electron microscopy (see Fig S2).

The roughness factors (R_f) of different Cu catalysts were calculated by normalizing the double-layer capacitance (C_{dl}) of each catalyst deposited onto carbon paper to that of reference Cu (Cu foil). Cu foil was polished with sandpaper then cleaned in 1 M HCl solution prior to measurement for removing oxide layers. Toray carbon paper (Fuel Cell Store) was used to deposit catalyst layer in order to minimize the contribution of microporous layer capacitance of Sigracet 39 BB GDL during the measurement. 0.1 mg cm⁻² of Cu particles were loaded on Toray carbon paper. The measurement was performed in a 0.1 M HClO₄-filled H-cell separated by a Nafion membrane with constant inert gas flowing. Multiple scans of cyclic voltammetry at various scan rates (50 to 200 mV s⁻¹) were performed by scanning a non-faradaic potential window of Cu (-0.2 to -0.1 V vs. Ag/AgCl) using a platinum wire as a counter electrode and Ag/AgCl (Pine Research) reference electrode. Then, C_{dl} was obtained from the slope of the geometric current density measured vs. the scan rate. The roughness factor R_f was normalized with its loading giving \tilde{R}_f .

$$\tilde{R}_{(f,\text{catalyst})} = \frac{C_{(dl,\text{catalyst})}}{C_{(dl,\text{Cu foil})}} \times \frac{1}{\text{Reference loading}(0.1\,\text{mg cm}^{-2})}$$
(2)

DFT calculations

DFT calculations were conducted using the BEEF-vdW⁵⁶ exchange-correlation functional. All thermodynamics were computed with GPAW^{57,58} where an electrochemical environment was mimicked using a hybrid explicit/implicit solvation scheme including a static water layer. ⁴¹ Our GPAW results compared well with results obtained in QuantumEspresso⁵⁹ in combination with the self-consistent continuum solvation (SCCS) model. ⁶⁰ Electrochemical reaction thermodynamics were referenced via the computational hydrogen electrode (CHE). ⁶¹ We applied the corrections by Christensen *et al.* to mitigate systematic DFT errors. ⁴⁸ Free energies were obtained following the ideal gas law for gas phase species and the harmonic oscillator model for adsorbates, respectively. All possible surface adsorbates were thoroughly sampled for their most stable adsorption site on each Cu facet using the package CatKit package. ⁶² From this sampling intermediates prior to HCCO* were selected for each reduction stage according to their thermodynamic stability which is also in line with established kinetic trends ⁴⁰ (see final path in Fig. S12). The grand canonical PCET barriers

where computed in alkaline conditions (H₂O as proton donor) using the Solvated Jellium Model (SJM)^{41,63} including an explicit water layer. We note that the calculations of electrochemical barriers still bear some uncertainties, ^{64,65} so we cautiously take these results as tentative. However, we note that the calculation of alkaline PCET barriers in this work was only possible via the use of this grand canonical framework, due to spontaneous coadsorption of OH⁻ in conventional transition state searches. For handling of atomic structures, geometry optimizations, vibration calculations and nudged-elastic-band (NEB)⁶⁶ calculations, the Atomic Simulation Environment (ASE) package⁶⁷ was used. For further details of DFT calculations, slab models and convergence criteria see SI Sec. 2.

Coupled microkinetic and transport model

The microkinetic model was solved for its steady-state using an ODE solver available in the SciPy distribution. ⁶⁸ Lateral interactions were ignored as they appear insensitive to the investigated mechanism (see SI Sec. 5.6.3). The mass transport followed a hierarchical multiscale model where the transport within a short diffusion length from the catalyst surface is solved via a 1-D model employing the electro-neutral Nernst-Planck equation ^{43,69} and outside of this diffusion length described by effective mass transport relations. 44-46 The transport of CO was assumed solely from the gaseous side and solved analytically with a short diffusion layer of 150 nm, necessary to achieve the high current densities (see Fig. 4). On the gaseous side the partial pressure of CO was assumed with 1 atm and it's aqueous solubility by the Henry constant. ⁷⁰ The transport of OH⁻ and H₂CCO and their solution reaction was numerically solved for a diffusion length of 1 μ m. Based on available experimentally determined constants employed in the model (see SI Sec. 5.2), the solution reaction is completed within this diffusion length (see Fig. 5a). Beyond the diffusion layer of 1 μ m conditions equivalent to the electrode/electrolyte interface are assumed where the OH⁻ concentration is determined through a Sherwood relation describing the flow perpendicular to the catalyst surface. 45,46 The microkinetic and transport models are iteratively solved for the catalyst surface concentrations. More details about the transport coupled microkinetic model can be found in the SI Sec. 5.

Code & Data availability

The code for the coupled microkinetic and transport model with all input data used in this work as well as the digitized data from Fig. 1 is available under the MIT License (https://opensource.org/licenses/MIT) and CC BY 4.0 (https://creativecommons.org/licenses/by/4.0/), respectively, in Zenodo (https://doi.org/10.5281/zenodo.5013854).

Conflicts of interest

There are no conflicts of interest to declare.

Acknowledgments

The research leading to these results has received funding from the European Union's Horizon 2020 research and innovation programme under grant agreement No 851441, SELECTCO2. Financial support was provided by V- Sustain: The VILLUM Centre for the Science of Sustainable Fuels and Chemicals (#9455) from VILLUM FONDEN. The authors acknowledge PRACE for awarding them access to the JUWELS supercomputer at GCS@FZJ in Germany through project 2020235596. The authors at the University of Delaware thank the National Science Foundation for financial support (Award No. CBET-1904966).

References

1. Nitopi, S.; Bertheussen, E.; Scott, S. B.; Liu, X.; Engstfeld, A. K.; Horch, S.; Seger, B.; Stephens, I. E.; Chan, K.; Hahn, C.; Nørskov, J.; Jaramillo, T. F.; Chorkendorff, I.

- Progress and perspectives of electrochemical CO2 reduction on copper in aqueous electrolyte. *Chem. Rev.* **2019**, *119*, 7610–7672.
- 2. Jouny, M.; Luc, W.; Jiao, F. General techno-economic analysis of CO2 electrolysis systems. *Ind. Eng. Chem. Res.* **2018**, *57*, 2165–2177.
- 3. De Luna, P.; Hahn, C.; Higgins, D.; Jaffer, S. A.; Jaramillo, T. F.; Sargent, E. H. What would it take for renewably powered electrosynthesis to displace petrochemical processes? *Science* **2019**, *364*.
- 4. Jouny, M.; Luc, W.; Jiao, F. High-rate electroreduction of carbon monoxide to multicarbon products. *Nat. Catal.* **2018**, *1*, 748–755.
- 5. Dinh, C.-T.; Burdyny, T.; Kibria, M. G.; Seifitokaldani, A.; Gabardo, C. M.; De Arquer, F. P. G.; Kiani, A.; Edwards, J. P.; De Luna, P.; Bushuyev, O. S.; Zou, C.; Quintero-Bermudez, R.; Pang, Y.; Sinton, D.; Sargent, E. H. CO2 electroreduction to ethylene via hydroxide-mediated copper catalysis at an abrupt interface. *Science* 2018, 360, 783–787.
- Burdyny, T.; Smith, W. A. CO₂ reduction on gas-diffusion electrodes and why catalytic performance must be assessed at commercially-relevant conditions. *Energy Environ. Sci.* 2019, 12, 1442–1453.
- 7. Li, C. W.; Kanan, M. W. CO2 reduction at low overpotential on Cu electrodes resulting from the reduction of thick Cu2O films. J. Am. Chem. Soc. 2012, 134, 7231–7234.
- 8. Li, C. W.; Ciston, J.; Kanan, M. W. Electroreduction of carbon monoxide to liquid fuel on oxide-derived nanocrystalline copper. *Nature* **2014**, *508*, 504–507.
- Kas, R.; Yang, K.; Bohra, D.; Kortlever, R.; Burdyny, T.; Smith, W. A. Electrochemical CO₂ reduction on nanostructured metal electrodes: fact or defect? *Chem. Sci.* 2020, 11, 1738–1749.

- 10. Resasco, J.; Bell, A. T. Electrocatalytic CO₂ reduction to fuels: progress and opportunities. *Trends Chem.* **2020**, *2*, 825–836.
- 11. Luc, W.; Fu, X.; Shi, J.; Lv, J.-J.; Jouny, M.; Ko, B. H.; Xu, Y.; Tu, Q.; Hu, X.; Wu, J.; Yue, Q.; Jiao, F.; Kang, Y. Two-dimensional copper nanosheets for electrochemical reduction of carbon monoxide to acetate. *Nat. Catal.* **2019**, *2*, 423–430.
- 12. Zhu, P.; Xia, C.; Liu, C.-Y.; Jiang, K.; Gao, G.; Zhang, X.; Xia, Y.; Lei, Y.; Alshareef, H. N.; Senftle, T. P.; Wang, H. Direct and continuous generation of pure acetic acid solutions via electrocatalytic carbon monoxide reduction. *Proc. Natl. Acad. Sci. U.S.A.* 2020, 118.
- Wang, Y.; Shen, H.; Livi, K. J.; Raciti, D.; Zong, H.; Gregg, J.; Onadeko, M.; Wan, Y.;
 Watson, A.; Wang, C. Copper nanocubes for CO₂ reduction in gas diffusion electrodes.
 Nano Lett. 2019, 19, 8461–8468.
- 14. Jouny, M.; Lv, J.-J.; Cheng, T.; Ko, B. H.; Zhu, J.-J.; Goddard, W. A.; Jiao, F. Formation of carbon–nitrogen bonds in carbon monoxide electrolysis. *Nat. Chem.* **2019**, *11*, 846–851.
- 15. Hall, A. S.; Yoon, Y.; Wuttig, A.; Surendranath, Y. Mesostructure-induced selectivity in CO2 reduction catalysis. *J. Am. Chem. Soc.* **2015**, *137*, 14834–14837.
- 16. Weng, L.-C.; Bell, A. T.; Weber, A. Z. Modeling gas-diffusion electrodes for CO₂ reduction. *Phys. Chem. Chem. Phys.* **2018**, *20*, 16973–16984.
- 17. Suter, S.; Haussener, S. Optimizing mesostructured silver catalysts for selective carbon dioxide conversion into fuels. *Energy Environ. Sci.* **2019**, *12*, 1668–1678.
- 18. Raciti, D.; Mao, M.; Wang, C. Mass transport modelling for the electroreduction of CO2 on Cu nanowires. *Nanotechnology* **2017**, *29*, 044001.

- 19. Bohra, D.; Chaudhry, J. H.; Burdyny, T.; Pidko, E. A.; Smith, W. A. Modeling the electrical double layer to understand the reaction environment in a CO2 electrocatalytic system. *Energy Environ. Sci.* **2019**, *12*, 3380–3389.
- Jang, J.; Rüscher, M.; Winzely, M.; Morales-Guio, C. G. Gastight Rotating Cylinder Electrode: Towards Decoupling Mass Transport and Intrinsic Kinetics in Electrocatalysis. AIChE J. 2021, e17605.
- Seidel, Y.; Schneider, A.; Jusys, Z.; Wickman, B.; Kasemo, B.; Behm, R. Mesoscopic mass transport effects in electrocatalytic processes. Faraday Discuss. 2009, 140, 167– 184.
- 22. Clark, E. L.; Resasco, J.; Landers, A.; Lin, J.; Chung, L.-T.; Walton, A.; Hahn, C.; Jaramillo, T. F.; Bell, A. T. Standards and protocols for data acquisition and reporting for studies of the electrochemical reduction of carbon dioxide. ACS Catal. 2018, 8, 6560–6570.
- 23. Nørskov, J. K.; Studt, F.; Abild-Pedersen, F.; Bligaard, T. Fundamental Concepts in Heterogeneous Catalysis; John Wiley & Sons, Inc., 2014.
- 24. Scholten, F.; Nguyen, K.-L. C.; Bruce, J. P.; Heyde, M.; Roldan Cuenya, B. Identifying Structure—Selectivity Correlations in the Electrochemical Reduction of CO2: A Comparison of Well-Ordered Atomically Clean and Chemically Etched Copper Single-Crystal Surfaces. Angew. Chem. 2021, 133, 19318–19324.
- Ripatti, D. S.; Veltman, T. R.; Kanan, M. W. Carbon monoxide gas diffusion electrolysis that produces concentrated C2 products with high single-pass conversion. *Joule* 2019, 3, 240–256.
- 26. Zhang, J.; Luo, W.; Züttel, A. Self-supported copper-based gas diffusion electrodes for CO₂ electrochemical reduction. *J. Mater. Chem. A* **2019**, *7*, 26285–26292.

- 27. Ma, M.; Clark, E. L.; Therkildsen, K. T.; Dalsgaard, S.; Chorkendorff, I.; Seger, B. Insights into the carbon balance for CO₂ electroreduction on Cu using gas diffusion electrode reactor designs. *Energy Environ. Sci.* 2020, 13, 977–985.
- 28. De Gregorio, G. L.; Burdyny, T.; Loiudice, A.; Iyengar, P.; Smith, W. A.; Buonsanti, R. Facet-dependent selectivity of Cu catalysts in electrochemical CO2 reduction at commercially viable current densities. ACS Catal. 2020, 10, 4854–4862.
- 29. Wang, X.; Wang, Z.; de Arquer, F. P. G.; Dinh, C.-T.; Ozden, A.; Li, Y. C.; Nam, D.-H.; Li, J.; Liu, Y.-S.; Wicks, J.; Chen, Z.; Chi, M.; Chen, B.; Wang, Y.; Tam, J.; Howe, J. Y.; Proppe, A.; Todorovic, P.; Li, F.; Zhuang, T.-T. et al. Efficient electrically powered CO₂-to-ethanol via suppression of deoxygenation. Nat. Energy 2020, 5, 478–486.
- 30. (a) Bertheussen, E.; Verdaguer-Casadevall, A.; Ravasio, D.; Montoya, J. H.; Trimarco, D. B.; Roy, C.; Meier, S.; Wendland, J.; Nørskov, J. K.; Stephens, I. E.; Chorkendorff, I. Acetaldehyde as an intermediate in the electroreduction of carbon monoxide to ethanol on oxide-derived copper. Angew. Chem. Int. Ed. 2016, 128, 1472–1476;
 (b) Bertheussen, E.; Hogg, T. V.; Abghoui, Y.; Engstfeld, A. K.; Chorkendorff, I.; Stephens, I. E. Electroreduction of CO on polycrystalline copper at low overpotentials. ACS Energy Lett. 2018, 3, 634–640;
 (c) Wang, L.; Nitopi, S. A.; Bertheussen, E.; Orazov, M.; Morales-Guio, C. G.; Liu, X.; Higgins, D. C.; Chan, K.; Nørskov, J. K.; Hahn, C.; Jaramillo, T. F. Electrochemical carbon monoxide reduction on polycrystalline copper: Effects of potential, pressure, and pH on selectivity toward multicarbon and oxygenated products. ACS Catal. 2018, 8, 7445–7454.
- 31. Wang, L.; Nitopi, S.; Wong, A. B.; Snider, J. L.; Nielander, A. C.; Morales-Guio, C. G.; Orazov, M.; Higgins, D. C.; Hahn, C.; Jaramillo, T. F. Electrochemically converting carbon monoxide to liquid fuels by directing selectivity with electrode surface area. *Nat. Catal.* **2019**, *2*, 702–708; (a) Raciti, D.; Cao, L.; Livi, K. J.; Rottmann, P. F.; Tang, X.; Li, C.; Hicks, Z.; Bowen, K. H.; Hemker, K. J.; Mueller, T.; Wang, C. Low-overpotential

- electroreduction of carbon monoxide using copper nanowires. ACS Catal. 2017, 7, 4467–4472.
- 32. Kuhl, K. P.; Cave, E. R.; Abram, D. N.; Jaramillo, T. F. New insights into the electrochemical reduction of carbon dioxide on metallic copper surfaces. *Energy Environ. Sci.* **2012**, *5*, 7050–7059.
- 33. Huang, Y.; Handoko, A. D.; Hirunsit, P.; Yeo, B. S. Electrochemical reduction of CO2 using copper single-crystal surfaces: effects of CO* coverage on the selective formation of ethylene. *ACS Catal.* **2017**, *7*, 1749–1756.
- 34. Andraos, J.; Kresge, A. J. Correlation of rates of uncatalyzed and hydroxide-ion catalyzed ketene hydration. A mechanistic application and solvent isotope effects on the uncatalyzed reaction. *Can. J. Chem.* **2000**, *78*, 508–515.
- 35. Schouten, K. J. P.; Pérez Gallent, E.; Koper, M. T. Structure sensitivity of the electrochemical reduction of carbon monoxide on copper single crystals. *ACS Catal.* **2013**, *3*, 1292–1295.
- 36. Montoya, J. H.; Shi, C.; Chan, K.; Nørskov, J. K. Theoretical insights into a CO dimerization mechanism in CO2 electroreduction. *J. Phys. Chem. Lett.* **2015**, *6*, 2032–2037.
- 37. Kastlunger, G.; Wang, L.; Govindarajan, N.; Heenen, H. H.; Ringe, S.; Jaramillo, T.; Hahn, C.; Chan, K. Using pH dependence to understand mechanisms in electrochemical CO reduction. *ACS Catal.* **2022**, *12*, 4344–4357.
- 38. Liu, X.; Schlexer, P.; Xiao, J.; Ji, Y.; Wang, L.; Sandberg, R. B.; Tang, M.; Brown, K. S.; Peng, H.; Ringe, S.; Hahn, C.; Jaramillo, T. F.; Nørskov, J. K.; Chan, K. pH effects on the electrochemical reduction of CO(2) towards C2 products on stepped copper. *Nat. Commun.* **2019**, *10*.

- 39. Govindarajan, N.; Kastlunger, G.; Heenen, H. H.; Chan, K. Improving the intrinsic activity of electrocatalysts for sustainable energy conversion: where are we and where can we go? *Chemical Science* **2022**, *13*, 14–26.
- 40. Patel, A. M.; Vijay, S.; Kastlunger, G.; Nørskov, J. K.; Chan, K. Generalizable Trends in Electrochemical Protonation Barriers. *J. Phys. Chem. Lett.* **2021**, *12*, 5193–5200.
- 41. Kastlunger, G.; Lindgren, P.; Peterson, A. A. Controlled-potential simulation of elementary electrochemical reactions: Proton discharge on metal surfaces. *J. Phys. Chem. C* **2018**, *122*, 12771–12781.
- 42. Overa, S.; Crandall, B.; Shrimant, B.; Tian, D.; Ko, B. H.; Shin, H.; Bae, C.; Jiao, F. Enhancing acetate selectivity by coupling anodic oxidation in carbon monoxide electroreduction. **2022**,
- 43. Subramaniam, A.; Chen, J.; Jang, T.; Geise, N. R.; Kasse, R. M.; Toney, M. F.; Subramanian, V. R. Analysis and simulation of one-dimensional transport models for lithium symmetric cells. *J. Electrochem. Soc.* **2019**, *166*, A3806.
- 44. Bohra, D.; Chaudhry, J.; Burdyny, T.; Pidko, E.; Smith, W. Mass Transport in Catalytic Pores of GDE-Based CO2 Electroreduction Systems. **2020**,
- 45. Modestino, M. A.; Hashemi, S. M. H.; Haussener, S. Mass transport aspects of electrochemical solar-hydrogen generation. *Energy Environ. Sci.* **2016**, *9*, 1533–1551.
- 46. Cussler, E. L.; Cussler, E. L. *Diffusion: mass transfer in fluid systems*; Cambridge university press, 2009.
- 47. Resasco, J.; Chen, L. D.; Clark, E.; Tsai, C.; Hahn, C.; Jaramillo, T. F.; Chan, K.; Bell, A. T. Promoter effects of alkali metal cations on the electrochemical reduction of carbon dioxide. J. Am. Chem. Soc. 2017, 139, 11277–11287.

- 48. Christensen, R.; Hansen, H. A.; Vegge, T. Identifying systematic DFT errors in catalytic reactions. *Catal. Sci. Technol.* **2015**, *5*, 4946–4949.
- 49. Strmcnik, D.; Uchimura, M.; Wang, C.; Subbaraman, R.; Danilovic, N.; Van Der Vliet, D.; Paulikas, A. P.; Stamenkovic, V. R.; Markovic, N. M. Improving the hydrogen oxidation reaction rate by promotion of hydroxyl adsorption. *Nat. Chem.* 2013, 5, 300.
- 50. Hori, Y. i. Modern aspects of electrochemistry; Springer, 2008; pp 89–189.
- 51. Birdja, Y. Y.; Koper, M. T. The importance of cannizzaro-type reactions during electrocatalytic reduction of carbon dioxide. *J. Am. Chem. Soc.* **2017**, *139*, 2030–2034.
- 52. Lum, Y.; Cheng, T.; Goddard III, W. A.; Ager, J. W. Electrochemical CO reduction builds solvent water into oxygenate products. J. Am. Chem. Soc. 2018, 140, 9337–9340.
- 53. Clark, E. L.; Wong, J.; Garza, A. J.; Lin, Z.; Head-Gordon, M.; Bell, A. T. Explaining the incorporation of oxygen derived from solvent water into the oxygenated products of CO reduction over Cu. J. Am. Chem. Soc. 2019, 141, 4191–4193.
- 54. Hasa, B.; Jouny, M.; Ko, B. H.; Xu, B.; Jiao, F. Flow Electrolyzer Mass Spectrometry with a Gas-Diffusion Electrode Design. *Angew. Chem. Int. Ed.* **2020**, *133*, 3314–3319.
- 55. Lu, X.; Zhao, C. Electrodeposition of hierarchically structured three-dimensional nickel—iron electrodes for efficient oxygen evolution at high current densities. *Nat. Commun.* **2015**, *6*, 6616.
- 56. Wellendorff, J.; Lundgaard, K. T.; Møgelhøj, A.; Petzold, V.; Landis, D. D.; Nørskov, J. K.; Bligaard, T.; Jacobsen, K. W. Density functionals for surface science: Exchange-correlation model development with Bayesian error estimation. *Phys. Rev. B* 2012, 85, 235149.

- 57. Mortensen, J. J.; Hansen, L. B.; Jacobsen, K. W. Real-space grid implementation of the projector augmented wave method. *Phys. Rev. B* **2005**, *71*, 035109.
- 58. Enkovaara, J.; Rostgaard, C.; Mortensen, J. J.; Chen, J.; Dułak, M.; Ferrighi, L.; Gavnholt, J.; Glinsvad, C.; Haikola, V.; Hansen, H. A.; Kristoffersen, H. H.; Kuisma, M.; Larsen, A. H.; Lehtovaara, L.; Ljungberg, M.; Lopez-Acevedo, O.; Moses, P. G.; Ojanen, J.; Olsen, T.; Petzold, V. et al. Electronic structure calculations with GPAW: a real-space implementation of the projector augmented-wave method. J. Phys.: Condens. Matter 2010, 22, 253202.
- 59. Giannozzi, P.; Baroni, S.; Bonini, N.; Calandra, M.; Car, R.; Cavazzoni, C.; Ceresoli, D.; Chiarotti, G. L.; Cococcioni, M.; Dabo, I.; Corso, A. D.; de Gironcoli, S.; Fabris, S.; Fratesi, G.; Gebauer, R.; Gerstmann, U.; Gougoussis, C.; Kokalj, A.; Lazzeri, M.; Martin-Samos, L. et al. QUANTUM ESPRESSO: a modular and open-source software project for quantum simulations of materials. J. Phys. Condens. Matter 2009, 21, 395502.
- 60. Andreussi, O.; Dabo, I.; Marzari, N. Revised self-consistent continuum solvation in electronic-structure calculations. *J. Chem. Phys.* **2012**, *136*, 064102.
- Nørskov, J.; Rossmeisl, J.; Logadottir, A.; Lindqvist, L.; Kitchin, J.; Bligaard, T.;
 Jónsson, H. Origin of the Overpotential for Oxygen Reduction at a Fuel-Cell Cathode.
 J. Phys. Chem. B 2004, 108, 17886–17892.
- Boes, J. R.; Mamun, O.; Winther, K.; Bligaard, T. Graph Theory Approach to High-Throughput Surface Adsorption Structure Generation. J. Phys. Chem. A 2019, 123, 2281–2285.
- 63. Lindgren, P.; Kastlunger, G.; Peterson, A. A. A Challenge to the G 0 Interpretation of Hydrogen Evolution. *ACS Catal.* **2019**, *10*, 121–128.

- 64. Gauthier, J. A.; Ringe, S.; Dickens, C. F.; Garza, A. J.; Bell, A. T.; Head-Gordon, M.; Nørskov, J. K.; Chan, K. Challenges in modeling electrochemical reaction energetics with polarizable continuum models. ACS Catal. 2018, 9, 920–931.
- 65. Gauthier, J. A.; Dickens, C. F.; Heenen, H. H.; Vijay, S.; Ringe, S.; Chan, K. Unified approach to implicit and explicit solvent simulations of electrochemical reaction energetics. *Journal of chemical theory and computation* 2019, 15, 6895–6906.
- 66. Lindgren, P.; Kastlunger, G.; Peterson, A. A. Scaled and Dynamic Optimizations of Nudged Elastic Bands. *Journal of chemical theory and computation* 2019, 15, 5787– 5793.
- 67. Larsen, A. H.; Mortensen, J. J.; Blomqvist, J.; Castelli, I. E.; Christensen, R.; Dułak, M.; Friis, J.; Groves, M. N.; Hammer, B.; Hargus, C.; Hermes, E. D.; Jennings, P. C.; Jensen, P. B.; Kermode, J.; Kitchin, J. R.; Kolsbjerg, E. L.; Kubal, J.; Kaasbjerg, K.; Lysgaard, S.; Maronsson, J. B. et al. The atomic simulation environment—a Python library for working with atoms. J. Phys. Condens. Matter 2017, 29, 273002.
- 68. Virtanen, P.; Gommers, R.; Oliphant, T. E.; Haberland, M.; Reddy, T.; Cournapeau, D.; Burovski, E.; Peterson, P.; Weckesser, W.; Bright, J.; van der Walt, S. J.; Brett, M.; Wilson, J.; Millman, K. J.; Mayorov, N.; Nelson, A. R. J.; Jones, E.; Kern, R.; Larson, E.; Carey, C. J. et al. SciPy 1.0: fundamental algorithms for scientific computing in Python. Nature methods 2020, 17, 261–272.
- 69. Heenen, H. H.; Voss, J.; Scheurer, C.; Reuter, K.; Luntz, A. C. Multi-ion conduction in Li3OCl glass electrolytes. *Journal Phys. Chem. Lett.* **2019**, *10*, 2264–2269.
- Sander, R. Compilation of Henry's law constants (version 4.0) for water as solvent.
 Atmos. Chem. Phys 2015, 15, 4399–4981.